Estimation of power performances and flow characteristics for a Savonius rotor by vortex particle method

Pan, Jingna; Ferreira, Carlos; van Zuijlen, Alexander

DOI
10.1002/we.2788

Publication date
2022

Document Version
Final published version

Published in
Wind Energy

Citation (APA)
Pan, J., Ferreira, C., & van Zuijlen, A. (2022). Estimation of power performances and flow characteristics for a Savonius rotor by vortex particle method. *Wind Energy*, *26*(1), 76-97. https://doi.org/10.1002/we.2788

Received: 16 February 2022 | Revised: 28 September 2022 | Accepted: 3 October 2022

DOI: 10.1002/we.2788

RESEARCH ARTICLE

WILEY

Estimation of power performances and flow characteristics for a Savonius rotor by vortex particle method

Jingna Pan | Carlos Ferreira | Alexander van Zuijlen

Faculty of Aerospace Engineering, Delft University of Technology, Delft, The Netherlands

Correspondence
Jingna Pan, Faculty of Aerospace Engineering, Delft University of Technology, Kluyverweg 1, 2629 HS, Delft, The Netherlands.
Email: J.Pan-1@tudelft.nl

Funding information
China Scholarship Council

Abstract

This study investigates the implementation of the vortex particle method (VPM) with the goal of efficiently and accurately estimating the power performances and flow characteristics for a Savonius rotor. The accuracy and efficiency of simulation methods are critical for the reliable design of Savonius rotors. Among various approaches, VPM is chosen because it can be flexibly incorporated with self-correction techniques, and the distribution of bound vortex particles can effectively represent complex geometries. In this work, a double-trailing-edge-wake-modeling vortex particle method (DTVPM) is presented to extend the working range of VPM for dealing with large rotating amplitudes and high tip speed ratios (TSRs). DTVPM addresses asymmetrical torque predictions for a Savonius rotor without gap width. However, DTVPM performs poorly at high TSRs due to the absence of viscous effects near the surface. To capture complex wake structures, such as reverse flow structures, the viscous correction for tip vortices is suggested. The current research focuses on the implementation and validation of DTVPM for predicting torque coefficients and wake patterns, as well as comparisons to OpenFOAM results. Two-dimensional and incompressible flow is estimated at $\lambda = 0.2–1.2$. For the studied cases, a maximum power coefficient is obtained at $\lambda \approx 0.8$, consistent with published experimental data. In addition, the process of trailing-edge vortices generation and detachment is captured by DTVPM. The comparison results between OpenFOAM and DTVPM show that DTVPM allows to efficiently simulate a Savonius rotor without any empirical parameters. DTVPM will help to improve existing engineering models for wind energy fields.

KEYWORDS
double-trailing-edge-wake-modeling, flow characteristics, power performances, Savonius rotor, vortex particle method

1 | INTRODUCTION

The Savonius rotor is one of the simplest wind turbines, consisting of at least two curved blades. Each blade has two sharp edges. Many geometrical parameters affect the operation of Savonius rotor, such as number of blades, gap width, number of stages, and blade shape. Early experimental

studies show that the recommended configuration is two stages of two twisted blades with a gap width of 0.1–0.15 from the point view of performance.[1,2] Because of cascade impact, the rotor performance decreases as the blade number increases from 2 to 3, as the adjacent blade affects the operation of the subsequent blade. The gap width affects the effective pressure on the advancing blade resulting in rotor performance variations. Multi-stage rotors and twisted blades are developed to reduce torque fluctuations so that the Savonius rotor can self-start at most angular positions without significant loss of power performance. With the prior knowledge of geometrical parameters, an optimal Savonius rotor is expected to be manufactured. The research issue is on a single-stage two-bladed semicircular Savonius rotor without gap width.

Apart from geometrical parameters, Savonius rotors are worth studying mainly due to their flexible operating conditions. They play an important role in the vertical axis wind turbine (VAWT) design field. The main advantage is that Savonius rotors can easily start up with high starting torque and low wind speeds of 2 to 3 m/s.[3,4] But in practice, a Savonius rotor can only achieve the maximum power coefficient (c_p) to a value lower than 0.25.[5–8] Darrieus rotors have high operational efficiency, but have difficulty in self-starting. Several researchers[9,10] have proposed a combined Darrieus–Savonius rotor to improve the turbine efficiency and obtain high starting torque. Prior knowledge of Savonius is necessary for the optimal design of a combined rotor. Unlike the Darrieus and horizontal axis wind turbines (HAWTs) which rely on round edged blades to ensure flow attachment, Savonius rotors involve more complex flow physics as a result of their consistent flow separation from two sharp edges. Over the last few decades, investigations about the two-dimensional (2D) unsteady inviscid incompressible flow behind an airfoil have caught wide attention in the engineering field.[11]

Accurately predicting the power performances, blade loads, and flow characteristics is significantly important for the efficient design of wind turbines. Several types of methodology have been used to study the physics of wind turbine blades. Theoretical work on the airfoil could date back to the 20th century. Lighthill[12] derived a thin airfoil theory for the distribution of the velocity field, rendering a valid approximation as a function of distance along the chord. Theodorsen[13] developed a potential flow solution for the unsteady flat plate with small pitch and plunge oscillations. Wagner[14] modeled the lift variation of an airfoil with a step change in angle of attack. Tollmien[15] and Lanchester[16] provided useful insights into how lift and drag develop on finite span wings by a lifting line theory. Although these classical theories have been proved valid and valuable for insights into unsteady aerodynamics, their feasibility is limited by assumptions of small amplitudes, fixed wake, etc. Advances in computational fluid dynamics (CFD) and experimental techniques have facilitated the detailed study and analysis of unsteady wake structures.

Experiments and high-fidelity computational methods have been used to address Savonius' unsteady flow problem. Korprasertsak[17] designed a wind booster for a Savonius rotor using XFLOW CFD software with Wall-Adapting Local-Eddy (WALE) turbulence model. This booster configuration improves the power efficiency and has a good agreement with experimental results. Kacprzak[18] examined the performance of conventional and modified Savonius rotors employing ANSYS CFX with shear stress transport (SST) k-ω turbulence model. Shigetomi[19] measured the flow field around multiple Savonius rotors using particle image velocimetry (PIV). Other high-fidelity methods, such as large eddy simulation (LES) and detached eddy simulation (DES), are expected to give more accurate predictions, especially on flow characteristics with massive flow separation. Gao[20] and Lee[21] studied the turbine performance and wake structures of a drag-type vertical axis hydrokinetic turbine using LES accompanied by a prototype experiment for validation. Although their simulations help to address step-by-step changes in the blade shape and operating tip speed ratio during optimization design process, it is reported in the literature that one simulation of 1.8 m long, 0.3 m wide and 0.54 m deep computational domain needs around 1800 h with 768 cores on the supercomputer. Dobrev[22] analyzed the performance and wake evolution of a Savonius rotor by means of unsteady Reynolds averaged Navier Stokes (URANS) and DES, revealing that the capability of DES gives more comparable rotor power and flow structures with experiments. Han[23] assessed improved delayed detached eddy simulation (IDDES) method in the supersonic flat plate boundary layer by comparing with two other hybrid RANS/LES methods. They recognized a limitation of IDDES that it underpredicted the mean skin friction in supersonic boundary layer flows. Elkhoury[24] studied effects of wind speed, aspect ratio, inflow angle on the performance of an orthopter-type VAWT using delayed detached eddy simulation (DDES). It is perceived that DDES can properly predict power coefficient of turbine along with the related 3D vortical flow structures. Antar[25] utilized 2D RANS and 3D DDES in the parametric optimization process for a Savonius rotor with guided plate configuration. Their results show that DDES can perfectly replicate the power performance curve and RANS can be seen as an alternative to avoid costly parametric processes. These numerical and experimental tools could give accurate predictions for unsteady flows. However, these CFD applications require extremely fine grids and large computational domains to get accurate solutions, and experimental techniques consume many resources in terms of equipment and construction. Both are inefficient concerning time and resources.

Therefore, the challenge is to develop a cost-effective method to simulate 2D unsteady inviscid incompressible flow behind an airfoil. As an alternative, the vortex-based methods are chosen to balance penalties and benefits between cost and fidelity.

Efforts have been put to predict complex flow separation of rotating blades using vortex methods. Ramesh[26] employed an inviscid theoretical method to non-periodic motions with a maximum pitching angle of 45° of a flat plate. But this model requires an empirical parameter, leading-edge suction parameter. Wang[27] proposed a low-order variable-strength vortex model (also called impulse matching model) by enforcing the Kutta condition at the leading and trailing edges. In their research, the vortex model could predict well for angles of attack up to 90°, but remains inadequate for aerodynamic control and estimation due to viscous and curvature effects referred by their later work.[28] Hemati[28] found a way to relax the Kutta conditions and determine the vortex strengths according to high-fidelity simulations. Ogawa[29] modeled the Savonius rotor by discrete vortex method. It is reported that the numerical results does not show a quantitative agreement with experiments, but yields a qualitative explanation to the wake pattern. Li and Calisal[30] proposed a discrete vortex method with free wake (DVM-UBC) to simulate the unsteady flow of

vertical axis tidal current turbines. It is presented that their method gives more accurate power performance than traditional DVM. But this method is highly dependent on the experimental data to calculate turbine's performance, such as force, torque and power coefficient. To reduce the dependency, they further developed DVM-UBC for quantitative predictions and utilized it to estimate turbine's characteristics.[31] Other computational effort[32] is to couple particle strength exchange (PSE) with immersed boundary vortex-in-cell (IB-VIC) methods. It includes the no-slip boundary conditions near blade surfaces to capture wake evolution and turbulent features of hydrokinetic turbines. However, the boundary layer flow is still not fully resolved.

It is worthwhile noted that aerodynamic investigations of single-stage two-bladed semicircular Savonius rotor without gap width using vortex particle method (VPM) have not been widely reported in literature. Despite the fact that unsteady flows have been reproduced behind a variety of structures, such as bridge sections, square sections, circular cylinder and triangular sections[33–35] by inserting vortex particles in predefined locations, it lacks of investigations focusing on flows around moving S-shaped bodies based on the vortex particle interactions and their contributions to rotor performances. Besides, there is no explicit implementation related to Savonius rotors in existing studies. When applying VPM to a Savonius rotor without gap width, mechanics of tip vortex shedding and bound vortex distribution need to be determined. If the whole rotor is considered as one body resembling the flat plate, the leading edge and trailing edge are then modeled using VPM. In this work, a double-trailing-edge-wake-modeling vortex particle method (DTVPM) is presented to adapt VPM for Savonius rotors without gap width. Because VPM cannot predict viscous flow due to the assumption of incompressible potential flow, the viscous effect is considered by a self-correction procedure for tip vortices in DTVPM. As a result, the implementation of DTVPM with viscous correction improves the accuracy of predictions, as will be discussed in the following sections.

This study focuses on elucidating DTVPM implementation and validate it against OpenFOAM. The modeling information is elaborated in Section 2. The proposed method is then applied to a Savonius rotor without gap width and compared with OpenFOAM and published experimental results in Section 3. The effects of tip speed ratio λ (TSR) and phase angle θ on power performances and flow characteristics are also investigated. Conclusions are discussed in Section 4.

2 | NUMERICAL PROCEDURE

2.1 | Principle of VPM

Schematic of the Savonius rotor is depicted in Figure 1. It includes two semicircular blades and a rotational axis located at the origin. The VPM is employed to simulate the incompressible flow around the 2D Savonius. It is based on the Navier-Stokes (NS) equation, describing fluid dynamics in the velocity $\vec{u}$ and vorticity $\vec{\omega}$ formulation at time t. For the incompressible inviscid flow, the continuity equation is given by Equation (1). The NS equation in terms of vorticity is written as Equation (2) assuming viscosity $\upsilon = 0$. According to the relation of circulation Γ and vorticity $\vec{\omega}$, the circulation can be defined as flux of voriticity through a specific surface, given by Equation (3). In the current 2D case, Γ is the vortex circulation in Z direction. With the distribution of circulations, the vorticity field can be obtained.

$$\nabla \cdot \vec{u} = 0 \tag{1}$$

$$\frac{\partial \vec{\omega}}{\partial t} + (\vec{u} \cdot \nabla)\vec{\omega} = \upsilon \nabla^2 \vec{\omega} = 0 \tag{2}$$

$$\Gamma = \int\int_S \vec{\omega} \cdot d\vec{S} \tag{3}$$

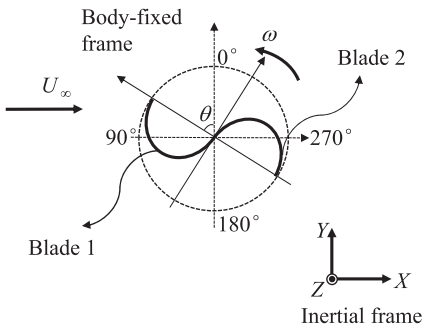

FIGURE 1 Schematic of a Savonius rotor

A brief introduction to VPM is also given in this section, emphasizing the specific details for the Savonius rotor. Interested readers may refer to *Low Speed Aerodynamics*[36] for extensive information. The distribution of vortex particles and the nomenclature of the Savonius rotor are depicted in Figure 2. A vortex element consists of end points $(x_a, y_a)(x_b, y_b)$, bound vortex point (x_v, y_v) at one-quarter chord from (x_a, y_a), and control point (x_c, y_c) at three-quarter chord from (x_a, y_a). Unit vectors $\vec{n}, \vec{\tau}$ are in the directions normal and tangential to the surface of the vortex element. β is the angle between element's normal and inflow directions. Δl is the vortex element's length. Γ_m, Γ_n represent bound vortex circulations of Blade 1 and Blade 2, respectively. Γ_{wake} is the latest shed vortex circulation.

To predict vortex characteristics, various vortex core models are compared in Section 3.2. Taking example of Vatistas model with order of 2,[37] the vortex-induced velocities in tangential and normal directions u, v by vortex point (x_v, y_v) are obtained in Equations (4) and (5), where r_c is the vortex core radius.

$$u = \frac{\Gamma}{2\pi} \frac{y_c - y_v}{\sqrt{\left((x_c - x_v)^2 + (y_c - y_v)^2\right)^2 + r_c^4}} \tag{4}$$

$$v = \frac{\Gamma}{2\pi} \frac{-(x_c - x_v)}{\sqrt{\left((x_c - x_v)^2 + (y_c - y_v)^2\right)^2 + r_c^4}} \tag{5}$$

The Neumann boundary condition should be satisfied at each control point as the fluid cannot go through a surface. By substituting the normal vortex-induced velocity at control point 1 into the Neumann boundary condition, Equation (6) is obtained with unknown circulations (Γ_{m_1}-Γ_{m_N}, Γ_{n_1}-Γ_{n_N}, Γ_{wake2}, Γ_{wake1}).

$$\begin{aligned} &a_{m_1 m_1}\Gamma_{m_1} + \ldots + a_{m_1 m_N}\Gamma_{m_N} + a_{m_1 n_1}\Gamma_{n_1} + \ldots + a_{m_1 n_N}\Gamma_{n_N} + \\ &a_{m_1 \text{wake2}}\Gamma_{\text{wake2}} + a_{m_1 \text{wake1}}\Gamma_{\text{wake1}} + (\vec{U} + \vec{U}_{\text{wake}} + \vec{U}_{\text{rot}}) \cdot \vec{n} = 0 \end{aligned} \tag{6}$$

In Equation (6), $a_{m_1 j}$ ($j = m_1$-m_N, n_1-n_N, wake1, wake2) is the influence coefficient of the normal velocity component induced by vortex element Γ_j, N is the number of vortex elements for one blade, $\vec{U}$ is the inflow velocity, $\vec{U}_{\text{wake}}$ is vortex-induced velocity by shed vortices (except the latest shed vortex), $\vec{U}_{\text{rot}}$ is rotational velocity. The last three terms are moved to the right hand side during implementation of VPM, given by $\text{RHS}_{m_1} = -(\vec{U} + \vec{U}_{\text{wake}} + \vec{U}_{\text{rot}}) \cdot \vec{n}$. Besides Neumann boundary condition, Kelvin condition also serves for the VPM because the time rate of circulation change in a closed curve should be conserved as zero, see Equation (7). In this equation, $\Gamma_{\text{b},t}, \Gamma_{\text{b},t-\Delta t}$ represent the sum of bound vortex circulations at current time t and previous time $t - \Delta t$.

$$\Gamma_{\text{b},t} + \Gamma_{\text{wake}} = \Gamma_{\text{b},t-\Delta t} \tag{7}$$

Assuming the bound and shed vortex elements' locations are known, the circulations' distribution is numerically solved and henceforth applied to aerodynamic computations. Meanwhile, a time stepping procedure is implemented in VPM, ensuring Kelvin condition and the Neumann boundary condition are satisfied at each time step.

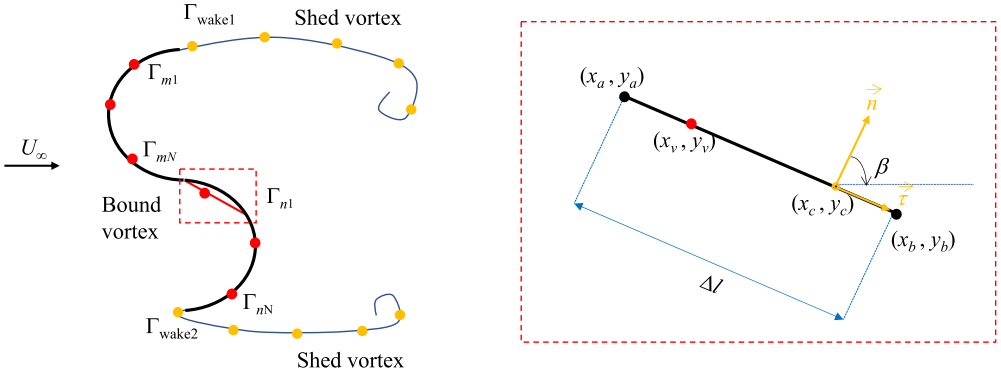

(A) Distribution of vortex particles (B) Nomenclature of vortex element

FIGURE 2 Schematic of bound and shed vortex particles [Colour figure can be viewed at wileyonlinelibrary.com]

However, the locations of leading and trailing edges of the rotating Savonius are ambiguous in VPM, since the two semicircular blades alternate during rotation. A self-correction technique is proposed by enabling two trailing edges at rotor tips in Section 2.2.

2.2 | DTVPM for Savonius

Each semicircular blade is discretized into N elements along the camber, representing the 2D Savonius in VPM. As shown in Figure 1, the two blades connect at the rotor center, resulting in two types of profile in Figure 3. In Figure 3A, the two blade tips are considered as a leading edge (LE) and a trailing edge (TE) in VPM. Control point and vortex point are distributed at the three-quarter and one-quarter of each vortex element, resulting in a fact that the positions of bound vortices at $\theta = 0^\circ$ will shift downwards at $\theta = 180^\circ$. According to the expression of normal vortex-induced velocity in Equation (5), any change of vortex points distribution will affect the influence coefficient at the control point. This asymmetrical rotation will cause inequivalent influence coeffecient and henceforth unbalanced force variations. Therefore, a symmetrical distribution is applied to avoid asymmetrical issues in Figure 3B, where two TEs are considered in the implementation of VPM, namely DTVPM. The influence coefficient from shed vortices will stay equivalent in the first and second 180° rotations. The results of two rotor profiles will be discussed in Section 3.

2.3 | Viscous correction for tip vortices

In this section, differences between viscous and inviscid flow physics from DTVPM are presented for a high-TSR case. The latest shed vortex is assumed to be located at a certain distance d from the blade tip, shown in Figure 3B. The distance is calculated by inflow velocity decomposed in the tangential direction of the closest vortex element $U_{,\tau}$ and time step size Δt in Equation (8), where constant f is chosen between 0.1 and 0.3.

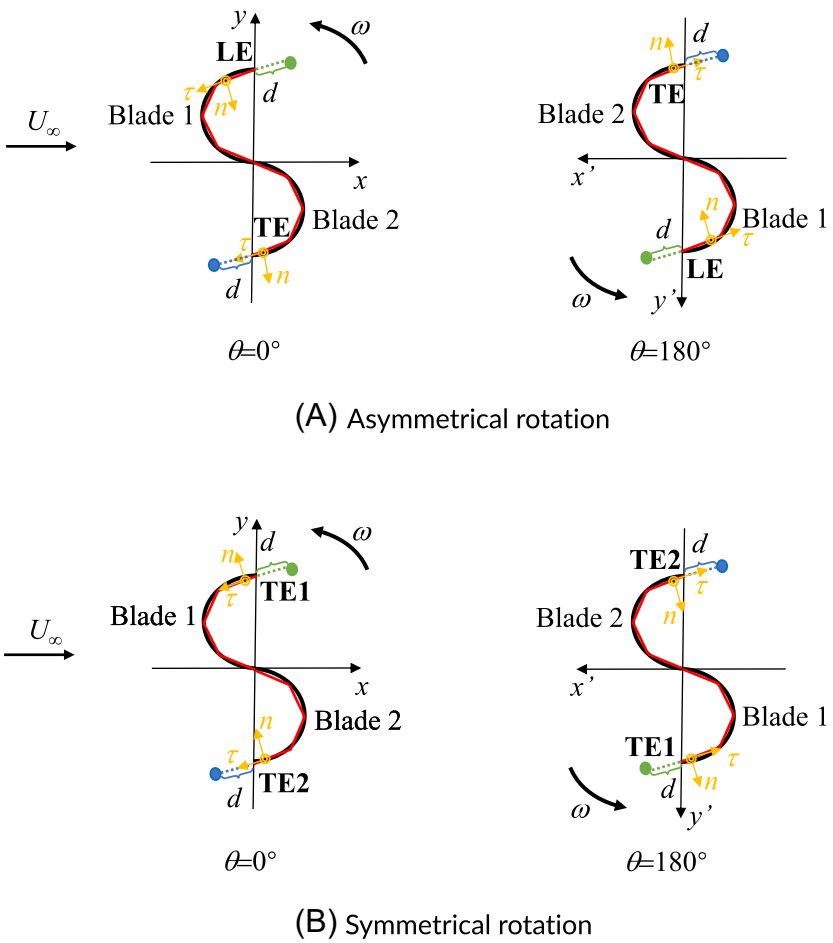

FIGURE 3 Two types of rotor profile [Colour figure can be viewed at wileyonlinelibrary.com]

$$d = fU_{,t}\Delta t \tag{8}$$

The latest shedding vortices play a key role in simulating flow features and predicting aerodynamic forces of the Savonius rotor. For low TSR, the vortex displacement $\vec{x}$ is commonly determined by local velocity[36] without considerations of viscosity, see Equation (9). While for high TSR, the effect of viscosity cannot be neglected especially near the blade surface. So, Equation (10) is applied to the near-wake region to correct tip vortex locations.

$$\frac{d\vec{x}}{dt} = \vec{u}(\mathbf{x}, t, \Gamma) \tag{9}$$

$$\frac{d\vec{x}}{dt} = \vec{u}(\vec{x}, t, \Gamma) + \vec{u}(\lambda) \tag{10}$$

In current work, the latest $5 \cdot \lambda$ (round to the closest integer) shed vortices (also called tip vortices) are relocated in different TSRs. Taking an example of $\lambda = 1.2$, the vortex trajectory without viscous correction is shown in Figure 4A, where the latest few particles follow the path of blade tips rotation. However, the flow pattern is quite different with viscous correction as shown in Figure 4B. The modified vortex trajectory could capture the typical flow structure, resulting in reasonable predictions of blade forces. Further comparisons can be found in Section 3.3.

2.4 | Aerodynamic calculations

According to the unsteady Bernoulli's equation, the pressure difference Δp of the surface is obtained from Equation (11).

$$\Delta p_j = \rho((U_\infty + u_{\text{vortex}}, v_{\text{vortex}})\vec{\tau_j}\frac{\Gamma_j}{\Delta l_j} + \vec{u}_{\text{rot}}\vec{\tau_j}\frac{\Gamma_j}{\Delta l_j} + \frac{\partial}{\partial t}\sum_{k=1}^{j}\Gamma_k) \tag{11}$$

The normal force F_n on the surface is obtained by integrating the pressure difference (per unit length) over the surface in Equation (12), including circulatory, kinematics, and added-mass effects.

$$F_n = \int_0^c \Delta p_j dc \tag{12}$$

In addition to the normal force, there is a leading-edge suction force acting on the surface, given by Blasius formula.[36] For a flat plate, the suction force (tangential force) pointing from leading edge to trailing edge is given by $\rho\pi c U_\infty^2 A_0^2$, where A_0 is Fourier coefficient, c is the chord length. In Figure 3B, the Savonius rotor is discretized into several vortex elements. If we consider each element as a flat plate, the suction force per unit length $F_{s,j}$ can be given by Equation (13). The torque Q on the Savonius rotor is calculated by forces and the force arm d_j in the form of Equation (14). The torque coefficient c_q is evaluated by dividing the torque with $\frac{1}{2}\rho U_\infty^2 DR$ in Equation (15), where D and R are rotor diameter and radius, respectively. The power coefficient c_p is given by Equation (16), where $\lambda = \frac{\Omega R}{U_\infty}$. Ω represents rotational speed.

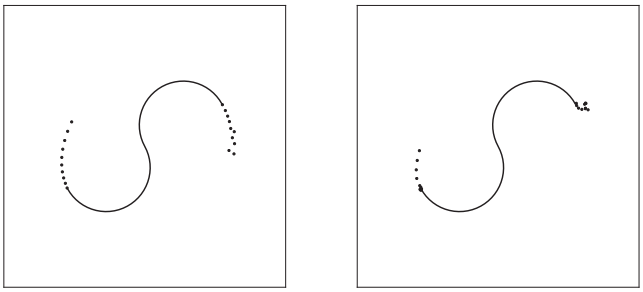

(A) Without viscous correction **(B)** With viscous correction

FIGURE 4 Tip vortex trajectory for $\lambda = 1.2$

$$F_{sj} = \rho \pi \Delta l_j U_\infty^2 (\sin \beta_j)^2 \tag{13}$$

$$Q = \sum_{j=1}^{2N} (F_{nj} \cdot \vec{n}_j d_j + F_{sj} \cdot \vec{\tau}_j d_j) \cdot \vec{e}_{\text{rot}} \tag{14}$$

$$c_q = \frac{Q}{\frac{1}{2}\rho U_\infty^2 DR} \tag{15}$$

$$c_p = c_q \cdot \lambda \tag{16}$$

2.5 | Implementation of DTVPM

The Savonius rotor's geometry and its motion kinematics are used as input in the implementation of DTVPM. Besides those two types of parameters, empirical data, like polar of lift-type turbines, are not required. This is a big advantage compared with other types of vortex methods, such as actuator line model, and lifting line model etc. The overall numerical procedure of DTVPM is depicted in Figure 5. As mentioned in Section 2.2, vortex-induced velocity is affected by the location of trailing edges. DTVPM is implemented to ensure equivalent influence coefficient and periodic force predictions. Once the distribution of vortices is determined, a linear system of equations can be built in Equation (17), representing the Neumann boundary condition (first 2*N* rows) and Kelvin theorem (last two rows). The wake shape is updated by a time stepping method.[36] In the implementation of DTVPM, viscous effects are corrected near blade tips.

$$\begin{pmatrix} a_{m_1m_1} & \cdots & a_{m_1m_N} & a_{m_1n_1} & \cdots & a_{m_1n_N} & a_{m_1\text{TE2}} & a_{m_1\text{TE1}} \\ \vdots & \ddots & \vdots & \vdots & \ddots & \vdots & \vdots & \vdots \\ a_{m_Nm_1} & \cdots & a_{m_Nm_N} & a_{m_Nn_1} & \cdots & a_{m_Nn_N} & a_{m_N\text{TE2}} & a_{m_N\text{TE1}} \\ a_{n_1m_1} & \cdots & a_{n_1m_N} & a_{n_1n_1} & \cdots & a_{n_1n_N} & a_{n_1\text{TE2}} & a_{n_1\text{TE1}} \\ \vdots & \ddots & \vdots & \vdots & \ddots & \vdots & \vdots & \vdots \\ a_{n_Nm_1} & \cdots & a_{n_Nm_N} & a_{n_Nn_1} & \cdots & a_{n_Nn_N} & a_{n_N\text{TE2}} & a_{n_N\text{TE1}} \\ 1 & \cdots & 1 & 0 & \cdots & 0 & 0 & 1 \\ 0 & \cdots & 0 & 1 & \cdots & 1 & 1 & 0 \end{pmatrix} \begin{pmatrix} \Gamma_{m_1} \\ \vdots \\ \Gamma_{m_N} \\ \Gamma_{n_1} \\ \vdots \\ \Gamma_{n_N} \\ \Gamma_{\text{TE2}} \\ \Gamma_{\text{TE1}} \end{pmatrix} = \begin{pmatrix} \text{RHS}_{m_1} \\ \vdots \\ \text{RHS}_{m_N} \\ \text{RHS}_{n_1} \\ \vdots \\ \text{RHS}_{n_N} \\ \Gamma_{b_1(t-\Delta t)} \\ \Gamma_{b_2(t-\Delta t)} \end{pmatrix} \tag{17}$$

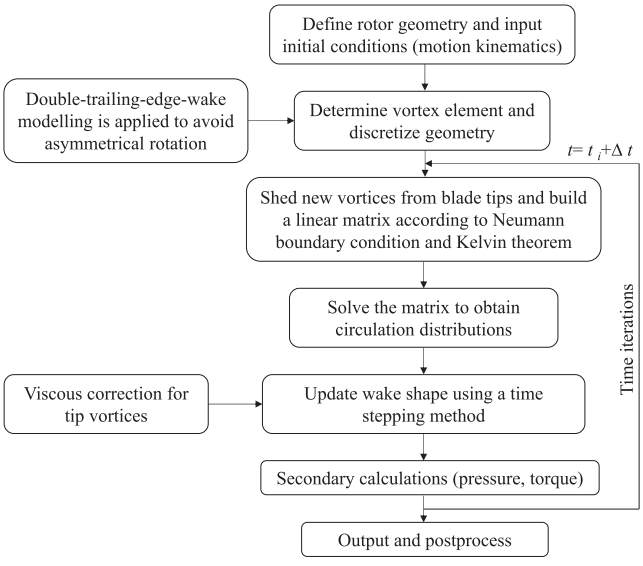

FIGURE 5 Flow chart of DTVPM

2.6 | OpenFOAM and experimental details

In this work, the OpenFOAM simulation is conducted to validate the proposed DTVPM. In OpenFOAM, the simulated Savonius rotor has the same geometry as in DTVPM, but with thickness of 0.001*D*. Tip speed ratios of 0.2–1.2 are employed with inflow velocity of 7 m/s. Although the Savonius rotor operates in a confined flow, its power performance and forces are insensitive to blockage effects when separated flow is presented.[38,39] As reported in literature,[39] turbines operating with blockage ratio of 10%–60% (larger than 6.67% in current work) at $\lambda = 1.4$ have a similar power performance and forces. The computational domain with blockage ratio of 6.67% is shown in Figure 6. The rotating axis is located at a distance of 15*R* from the inlet boundary. The whole domain is divided into the rotational and the stationary subdomains. The transfer of field variables across the domains is achieved through an arbitrary mesh interface (AMI). This study is based on URANS approach, in which SST $k-\omega$ turbulence model is employed to simulate the incompressible, viscous transient flow. A second-order upwind scheme is used for the spatial discretization of the momentum equations in the simulations. The first row's cell height of the outer boundary layer is 0.051 mm, calculated based on $y^+ = 1.0$. The angle interval (angle step size) for $\lambda = 0.2$–1.2 is chosen as 0.24°.

The experiments were conducted in the Vought Systems Division 4.9 m × 6.1 m Low Speed Wind Tunnel[1] to evaluate aerodynamic performance of a Savonius rotor. The presented results are power and torque coefficients as a function of tip speed ratio. Different parameters were studied in this experiment, including number of blades (2 and 3), gap width (0–0.1 m), and rotor height (1 and 1.5 m). The diameter of each blade is 0.5 m. All configurations were tested at inflow velocities of 7 and 14 m/s, respectively. A schematic of the Savonius rotor, instrumentation, load and control system is shown in Figure 7.

3 | RESULTS AND DISCUSSIONS

3.1 | Validation against OpenFOAM and experiments

The power coefficients c_p versus λ from OpenFOAM, experiment, DTVPM with and without viscous corrections are depicted in Figure 8. The variation trend of c_p increases from $\lambda = 0.2$ to $\lambda = 0.8$ and decreases from $\lambda = 0.8$ to $\lambda = 1.2$ in the three simulation methods, which is comparable with experimental results[1] for all TSRs. The maximum power output occurs at $\lambda \approx 0.8$. However, DTVPM without viscous correction underestimates c_p when $\lambda > 0.8$. Despite discrepancies of DTVPM without viscous correction, power coefficients from DTVPM with viscous correction, OpenFOAM and experiment are in a reasonable agreement. To validate the implementation of DTVPM, detailed results of DTVPM are compared with OpenFOAM simulations in the following sections.

In order to quantify the validation results of power coefficient, deviations of simulations for power coefficients at different TSRs are presented in Table 1. Δc_p is the difference between numerical and experimental results. It is observed that OpenFOAM and DTVPM with viscous correction predict more stable results for varied tip speed ratio with a standard deviation of 0.02. With the premise of stable prediction, OpenFOAM

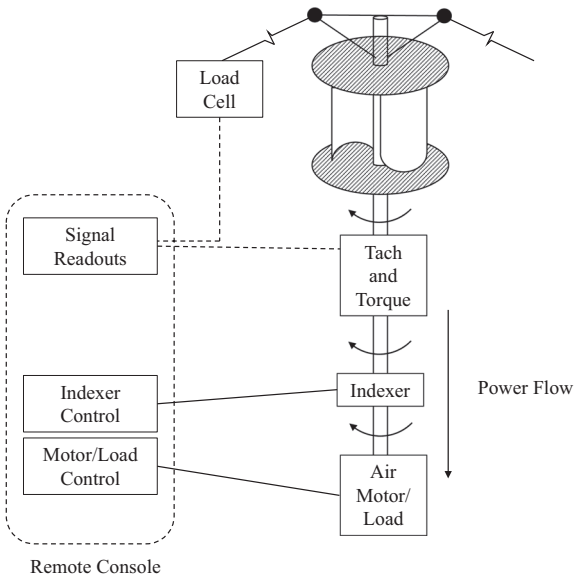

FIGURE 6 Schematic of the Savonius rotor/instrumentation load system[1]

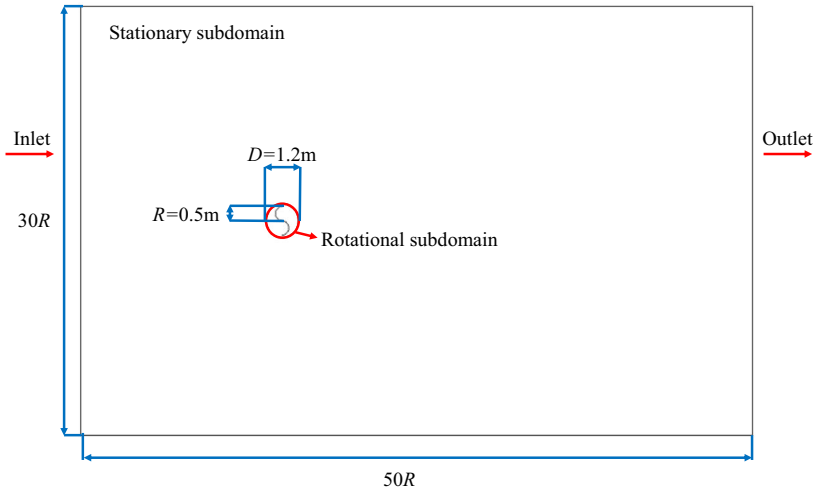

(A) Computational domain

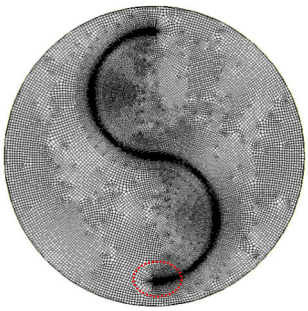

(B) Rotational subdomain

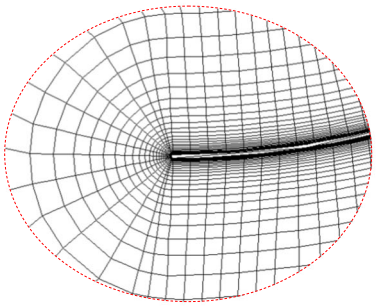

(C) Structured grid around the rotor

FIGURE 7 Computational domain and mesh for OpenFOAM simulation [Colour figure can be viewed at wileyonlinelibrary.com]

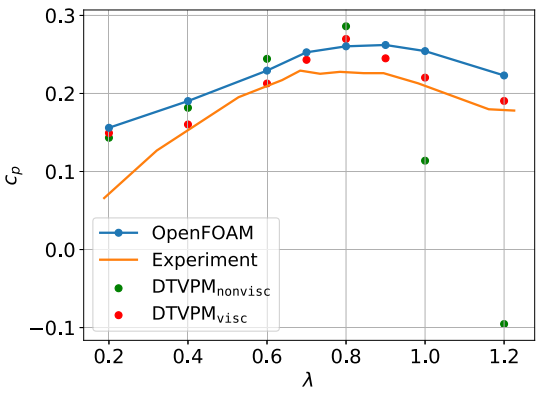

FIGURE 8 Power coefficient for different TSRs [Colour figure can be viewed at wileyonlinelibrary.com]

TABLE 1 Deviations of simulations for power coefficients at different TSRs

Δc_p	$\lambda = 0.2$	$\lambda = 0.4$	$\lambda = 0.6$	$\lambda = 0.8$	$\lambda = 1.0$	$\lambda = 1.2$	Standard deviation σ
OpenFOAM	0.08	0.04	0.02	0.03	0.04	0.04	0.02
DTVPM$_{nonvisc}$	0.07	0.03	0.03	0.06	−0.10	−0.27	0.12
DTVPM$_{visc}$	0.08	0.01	0.00	0.04	0.01	0.01	0.02

and DTVPM with viscous correction are prior to DTVPM without viscous correction. Among the two implementations of DTVPM, the viscous correction tends to predict more accurate c_p with Δc_p=0.01 for λ=1.0, 1.2.

3.2 | Sensitivity analysis and convergence study

For a rotating Savonius, a proper vortex core model has a significant effect on vortex interactions. Among all available vortex core models, a common approach for the vortex induced velocity $\vec{V}$ is using a desingularized algebraic profile with a constant vortex core size or a diffusive core growth with time. Hald[40] has proved that adjacent vortices distancing is a key parameter for the convergence of the vortex method. Hence, the vortex core radius needs to be compared and selected for the implementation of DTVPM. Kaufmann,[41] Vatistas,[37] and Lamb Oseen[42,43] models commonly overcome the singular nature of potential vortex. Kaufmann[41] model reduces the maximum induced velocity in the form of Equation (18). Vatistas[37] proposed a family of disingularized vortex core model with $n=1,2,3\ldots$, expressed as Equation (19). Lamb Oseen model[42,43] is developed to approximate the viscous core structure by taking the diffusion effect into account, expressed as Equation (20). r_{c0} is initial core radius at the origin of vortex. By differentiating Equation (20) concerning radial distance $\vec{r}$ and setting the derivative as zero, the viscous vortex core radius r_c is then obtained to grow with time as Equation (21), where the Oseen parameter $\sigma=1.25643$.[44]

$$\vec{V}=\frac{1}{2\pi}\frac{\vec{r}}{\vec{r}^{\,2}+r_c^2}\times\vec{e}_Z\Gamma \tag{18}$$

$$\vec{V}=\frac{1}{2\pi}\frac{\vec{r}}{\left(\vec{r}^{\,2n}+r_c^{2n}\right)^{1/n}}\times\vec{e}_Z\Gamma \quad (n=1,2,3\ldots) \tag{19}$$

$$\vec{V}=\frac{1}{2\pi\vec{r}}\left(1-e^{-\frac{\vec{r}^{\,2}}{4\upsilon t+r_{c0}^2}}\right)\times\vec{e}_Z\Gamma \tag{20}$$

$$r_c(t)=\sqrt{4\sigma\upsilon t+r_{c0}^2} \tag{21}$$

Figure 9 shows the induced velocity distributions on the basis of various vortex models. As Kaufmann model tends to underestimate induced velocities, Vatistas with $n=2$ and Lamb Oseen models have a similar trend except the vortex origin. As shown in the detail of Figure 9, Lamb Oseen model shows a smoother variation from the vortex origin to a finite radial distance than Vatistas model. The two models are further investigated and evaluated based on the downstream velocity, particle map, and torque coefficient. Vatistas model with $r_c=0.012, 0.022, 0.032$ m and Lamb Oseen model with $r_{c0}=0, 0.005, 0.01, 0.015$ m are employed. Figure 10 shows comparisons of downstream velocity for Vatistas and Lamb Oseen models at $\lambda=0.8$. As shown in Figure 10A,C, two vortex core models predict a similar velocity distribution in the near-wake region $x/R=2$. $\Delta(U/U_\infty)$ is the difference between DTVPM and OpenFOAM. Vatistas model with $r_c=0.012$ m has a maximum $\Delta(U/U_\infty)$ of 0.43 (0.65 while $r_c=0.022$ m) with a standard deviation of 0.08 (0.15 while $r_c=0.022$ m) at $x/R=2$. In the far-wake region $x/R=18$ of Figure 10B,D, Vatistas model with $r_c=0.012$ m differs from OpenFOAM in a maximum $\Delta(U/U_\infty)$ of 0.12 (0.26 while $r_c=0.022$ m) with a standard deviation of

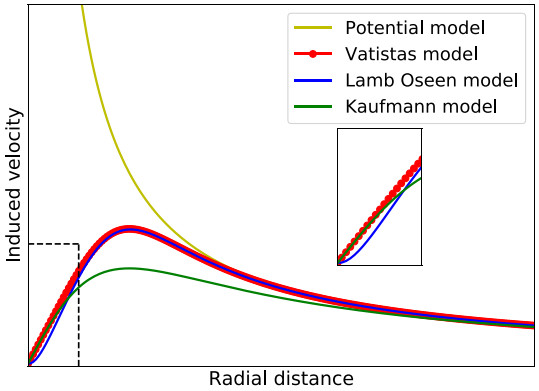

FIGURE 9 Vortex-induced velocity distribution of various vortex models [Colour figure can be viewed at wileyonlinelibrary.com]

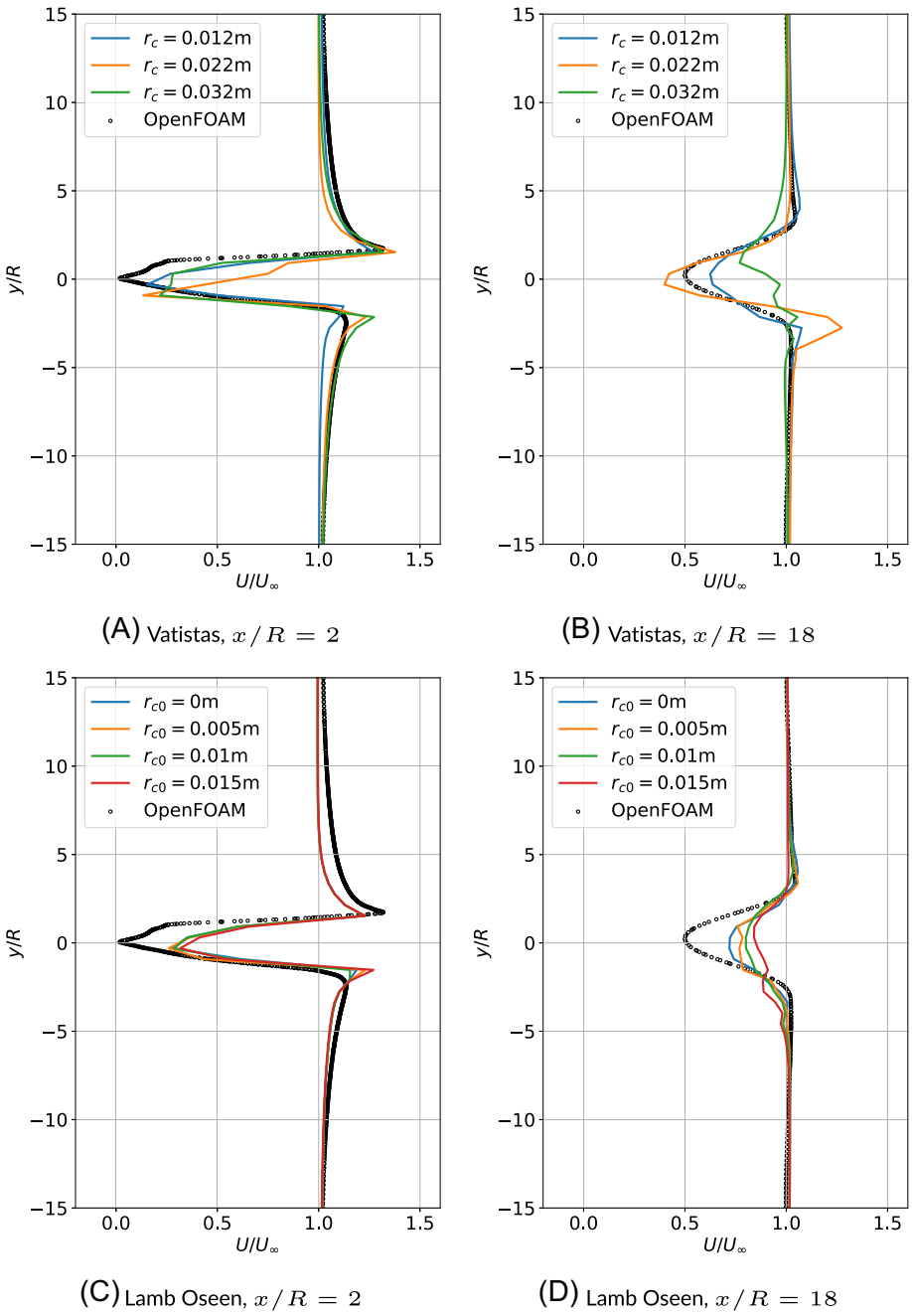

FIGURE 10 Sample downstream velocity curve for two vortex core models, $\lambda = 0.8$ [Colour figure can be viewed at wileyonlinelibrary.com]

0.03 (0.06 while $r_c = 0.022$ m). The maximum $\Delta(U/U_\infty)$ predicted by Lamb Oseen model differs from OpenFOAM by at least 0.37 with a standard deviation of 0.09 at $x/R = 2$, and at least 0.22 with a standard deviation of 0.05 at $x/R = 18$. To obtain a better prediction of downstream velocity fields, Vatistas model with $r_c = 0.012$ m is suggested when $\lambda = 0.8$.

Figures 11 and 12 present the effect of vortex core model on the particle map and torque coefficient c_q, respectively. It is observed that the vortex blobs are located at similar positions in the Lamb Oseen and Vatistas models. Additionally, both models estimate the periodic variation of the torque acting on the rotor with the largest $c_q \approx 1.0$. Table 2 lists power coefficients from different vortex core models and OpenFOAM. Vortex core radius of 0.024 m predicts a more comparable c_p with OpenFOAM. Although c_q from Vatistas model slightly fluctuates near $\theta = 30°$, the Vatistas model with $n = 2$ and $r_c = 0.024$ m is suggested for $\lambda = 0.8$ considering the wake profile and power performance predicted by the two vortex core models.

The power performances are further investigated in three different inflow conditions using DTVPM with viscous correction. Lamb Oseen[42,43] model is employed due to its viscous term. The inflow conditions are characterized by three Reynolds numbers: $Re \approx$ 2.86e5, 5.85e5 and 1.14e6.

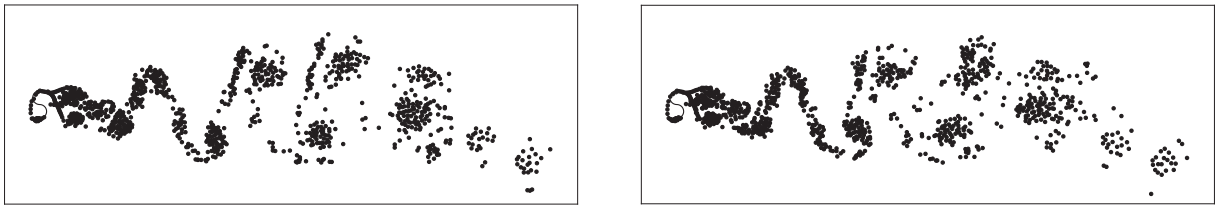

(A) Lamb Oseen (B) Vatistas

FIGURE 11 Effect of vortex core model on the particle map, $\lambda = 0.8$

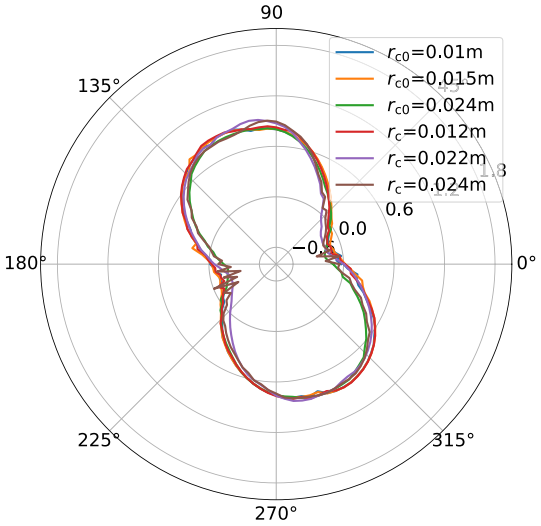

FIGURE 12 Effect of vortex core model on the torque coefficient c_q, $\lambda = 0.8$, Lamb Oseen: r_{c0}, Vatistas: r_c [Colour figure can be viewed at wileyonlinelibrary.com]

TABLE 2 Power coefficients from different vortex core models and OpenFOAM

	Lamb Oseen			Vatistas			OpenFOAM
r_c [m]	**0.01**	**0.015**	**0.024**	**0.012**	**0.022**	**0.024**	-
c_p	0.318	0.328	0.274	0.321	0.281	0.270	0.260

Figure 13 shows power coefficient c_p as a function of tip speed ratio (TSR) for Savonius rotor with various Reynolds numbers. It is observed that increasing Reynolds number appears to slightly increase c_p for majority TSRs. The dependence of Reynolds number has also been reported in previous studies,[1,4] and it is resulted from a delay of flow separation on the convex side of the rotor for a high Reynolds number.

The convergence study is performed based on the angle interval $\Delta\theta = 4.76° - 1.28°$. Their particle maps are shown in Figure 14. It is observed that the particle maps are converging to a specific distribution profile as $\Delta\theta$ decreases. To further study the convergence of DTVPM, the velocity variations at downstream are compared with OpenFOAM results in Figure 15. Four rotations are taken into account for each velocity curve. As observed in Figure 15, DTVPM predicts similar variation trends with OpenFOAM. In the near-wake region $x/R = 2$, the nondimensional velocity at $y/R \approx 1.5$ is much higher than that at $y/R \approx -1.5$. The asymmetry velocity variation is well captured by OpenFOAM and the four cases of DTVPM. This asymmetry could be consequence of staggered distributed vortex blobs in the x direction. DTVPM with $\Delta\theta = 3.60°$ differs from OpenFOAM in a maximum $\Delta(U/U)$ of 0.43 (same with $\Delta\theta = 1.28°$) and average $\Delta(U/U)$ of −0.01 (0.004 while $\Delta\theta = 1.28°$) with a standard deviation of 0.08 (0.09 while $\Delta\theta = 1.28°$) along the section of $x/R = 2$. For $x/R = 18$, the maximum and average $\Delta(U/U)$ predicted by DTVPM with $\Delta\theta = 3.60°$ are 0.12 and 0.02 (0.19 and 0.01 while $\Delta\theta = 1.28°$), respectively. The standard deviation of $\Delta(U/U)$ is 0.03 (0.05 while $\Delta\theta = 1.28°$). Even though decreasing $\Delta\theta$ from 3.60° to 1.28° may allow DTVPM to predict a bit more consistent results with OpenFOAM, the simulation will be more computationally expensive with smaller $\Delta\theta$. As mentioned above, because DTVPM with $\Delta\theta = 3.60°$ provides acceptable accuracy and computational efficiency, it is selected in the following cases.

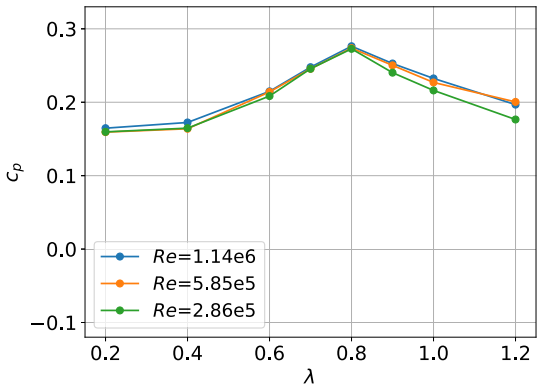

FIGURE 13 Power coefficient of Savonius rotor with different Reynolds numbers [Colour figure can be viewed at wileyonlinelibrary.com]

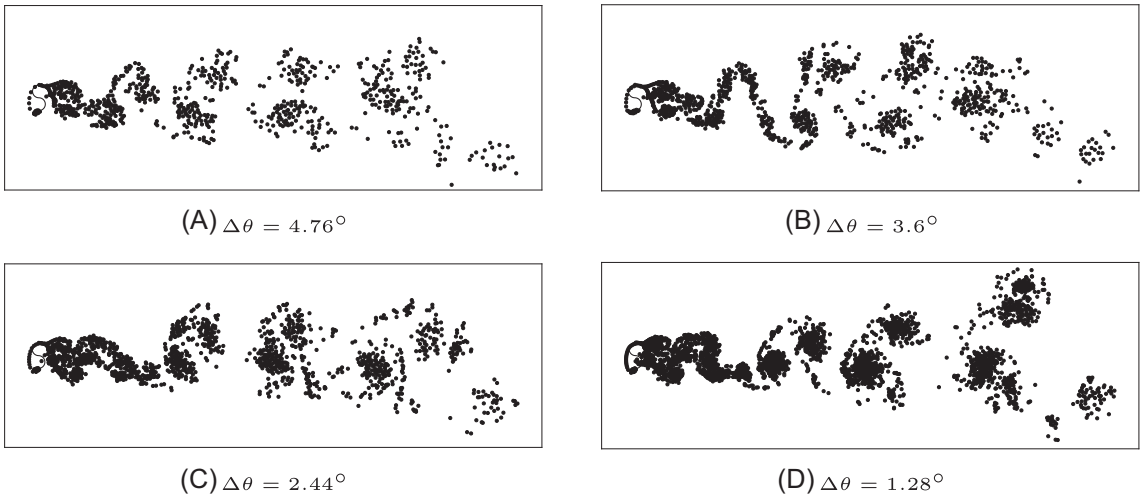

FIGURE 14 Particle maps after the fifth rotation, $\lambda = 0.8$

3.3 | Effect of viscous correction for tip vortices

This section is to verify the viscous corrections for tip vortices stated in Section 3.3. Figures 16 and 17 depict the inputs and effects of the vortex system corresponding to the optimized DTVPM with viscous correction and original DTVPM without correction for $\lambda = 1.2$. Figure 16 presents the vortex particle map at four phase angles. In these maps, the latest 10 vortex particles are displayed, showing notable differences between DTVPM with and without viscous effects near blade tips. In the viscous cases, the vortex particles shedding from trailing edges tend to recirculate back to the rotating directions. The viscous effects on the velocity field are shown in Figure 17. It compares the velocity fields from OpenFOAM, and DTVPM with and without viscous corrections at phase angle of 30°. The reverse flow mentioned above is also observed in velocity fields from OpenFOAM, shown in Figure 17A, which is expected in practical since there are significant viscous effects near the rotor. As shown in Figure 17B, the reverse flow near the bottom blade tip is well captured by the corrected method. But in Figure 17C, this phenomenon is not observed due to lack of roll up vortex particles. So the viscous correction for tip vortices is required for Savonius rotor with high TSRs.

3.4 | Effect of TSR

A comparison of the torque variation from OpenFOAM, VPM, and DTVPM with and without viscous effects near blade tips is shown in Figure 18. Table 3 lists standard deviation and maximum value of Δc_q over one revolution. As discussed in Section 2.2, the biggest difference between VPM and DTVPM is the distributions of TEs. Figure 18 shows that DTVPM with and without viscous corrections yield more symmetrical

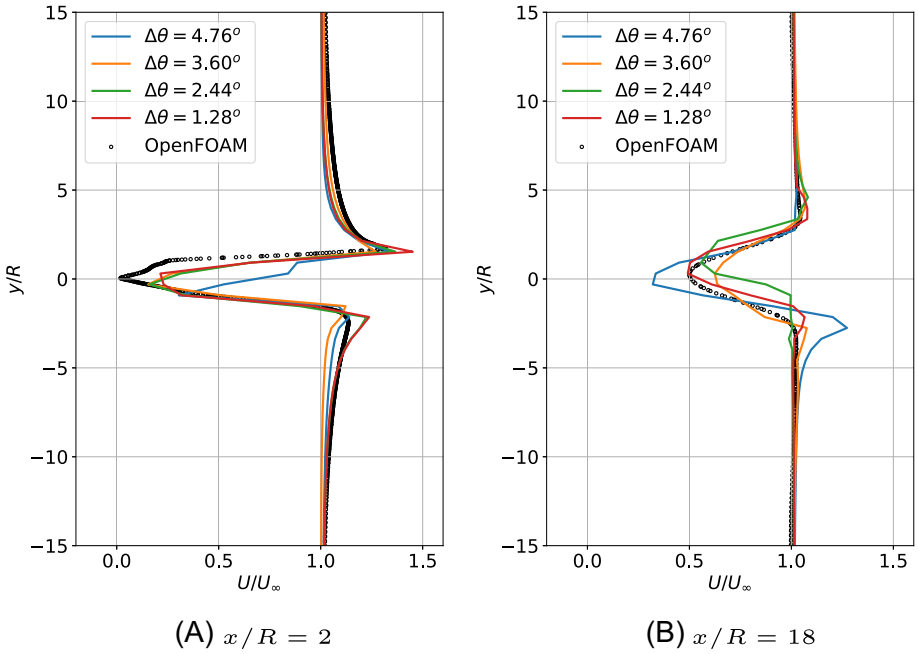

FIGURE 15 Sample downstream velocity curve for different angle intervals, $\lambda = 0.8$ [Colour figure can be viewed at wileyonlinelibrary.com]

torque predictions than VPM. During the second 180° rotation, VPM tends to overestimate/underestimate the torque on the rotor in a maximum difference of 0.65 with a standard deviation of 0.24, which are higher than the two implementations of DTVPM. Hence, for the simulation of rotating Savonius, it is essential to apply double-trailing-edge-wake-modeling to VPM.

Through comparison between DTVPM with and without viscous corrections in Figure 18 and Table 3, the proposed viscous corrections for tip vortices will insignificantly affect the accuracy of torque calculations at $\lambda < 1.0$. However, DTVPM without viscous correction at $\lambda = 1.2$ is different from OpenFOAM with a maximum difference of 0.83, which is greatly reduced to 0.44 when including viscous correction. The average standard deviations for the three implementations of VPM are 0.24, 0.16 and 0.20. Figure 18A depicts a phase shift of about 25° for torque coefficients of DTVPM without/with viscous corrections, resulting in an increase of standard deviation from 0.20 to 0.32/0.37.

3.5 | Effect of phase angle

DTVPM can also be utilized to learn flow characteristics behind Savonius rotor in an efficient way. In this section, the influence of the rotor phase angle is investigated by comparing OpenFOAM and DTVPM with viscous correction. Figure 19 depicts flow features over one revolution at $\lambda = 0.8$ with three downstream locations represented by dashed lines, $x/R = -2, 2, 18, 26$. The observations include:

- Vortex blobs have a staggered and periodic distribution that agrees with Kármán vortex street phenomenon, also appears in literature.[26]
- The near-wake region at $0 \le x/R \le 2$ is well predicted by DTVPM for vortex positions and velocity magnitude.
- The shedding vortices at far-wake region ($x/R \ge 2$) are found to be deflected with a larger amplitude in the y direction. It could be due to the neglect of viscous effects at downstream, which can be improved by employing particle strength exchange.

The vorticity fields at near-wake region are depicted in Figure 20. At $\theta = 160°$, the trailing-edge vorties (TEVs) start to appear at the two blade tips. As the rotor keeps rotating, the sizes of TEVs gradually grow and are large enough to be shed from the blade tips at $\theta = 240°$. Due to the symmetrical feature of rotation, when it rotates at around $\theta = 320°$, a new process of TEV generation and detachment start to alternate in the flow field. Through comparison of vorticity field from OpenFOAM and DTVPM, the near-wake flow characteristics are considered to be in a good agreement. The concentrated TEV blobs near the rotor are located at roughly the same positions. In addition, TEV generation near the driving blade (left blade in Figure 20A) tip causes reverse flow, which contributes to torque generation from $\theta = 80°$ to $\theta = 160°$. TEV detaches from the driving blade (top blade in Figure 20C) tip, restricting torque generation from $\theta = 160°$ to $\theta = 240°$.

To provide a more detailed analysis of the inflow and wake features, velocity curve variations at four downstream positions and five phase angles are presented in Figures 21–24. Figure 21 presents velocity curve variations in front of Savonius rotor. For given phase angles, the wake

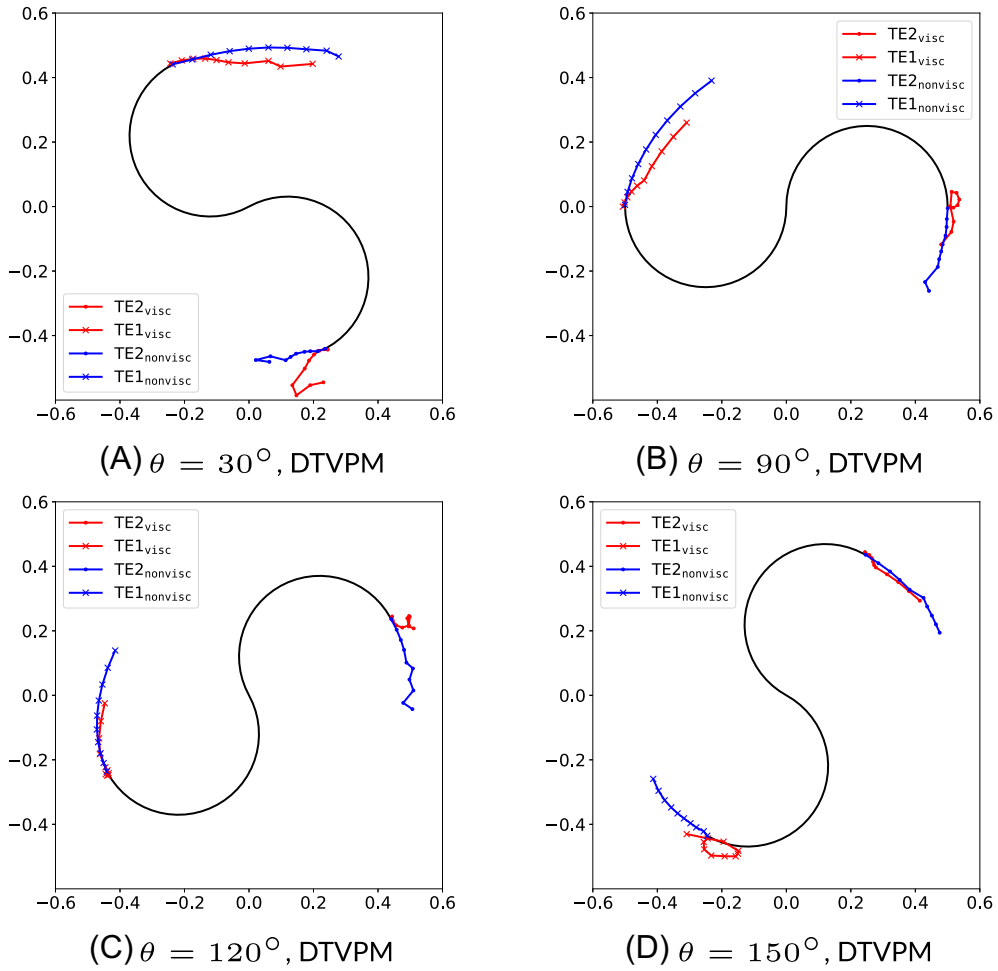

FIGURE 16 Latest 10 vortex particle trajectory from DTVPM with and without viscous corrections at $\lambda = 1.2$ [Colour figure can be viewed at wileyonlinelibrary.com]

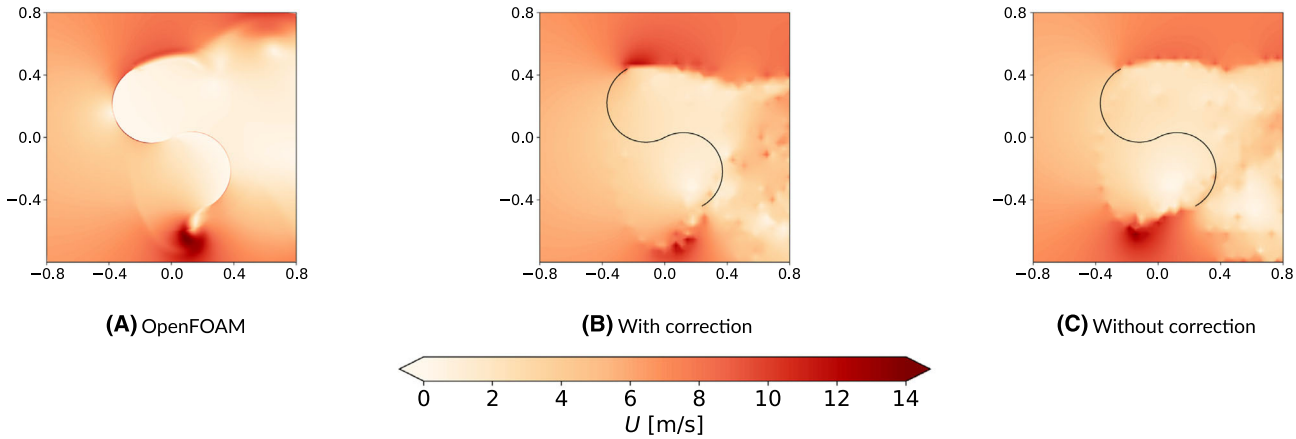

FIGURE 17 Velocity field from DTVPM with and without viscous corrections at $\theta = 30°, \lambda = 1.2$ [Colour figure can be viewed at wileyonlinelibrary.com]

width is well captured by DTVPM. In Figure 22, DTVPM and OpenFOAM can clearly capture the wake asymmetry. Figures 23 and 24 show that the wake profile at further downstream is dominated by instabilities of DTVPM, showing larger differences from OpenFOAM on the velocity curves. As shown in Figures 23D and 19D, DTVPM predicted a maximum $\Delta(U/U_\infty)$ of 0.31 with a standard deviation of 0.08 at x/R=18, θ=320°

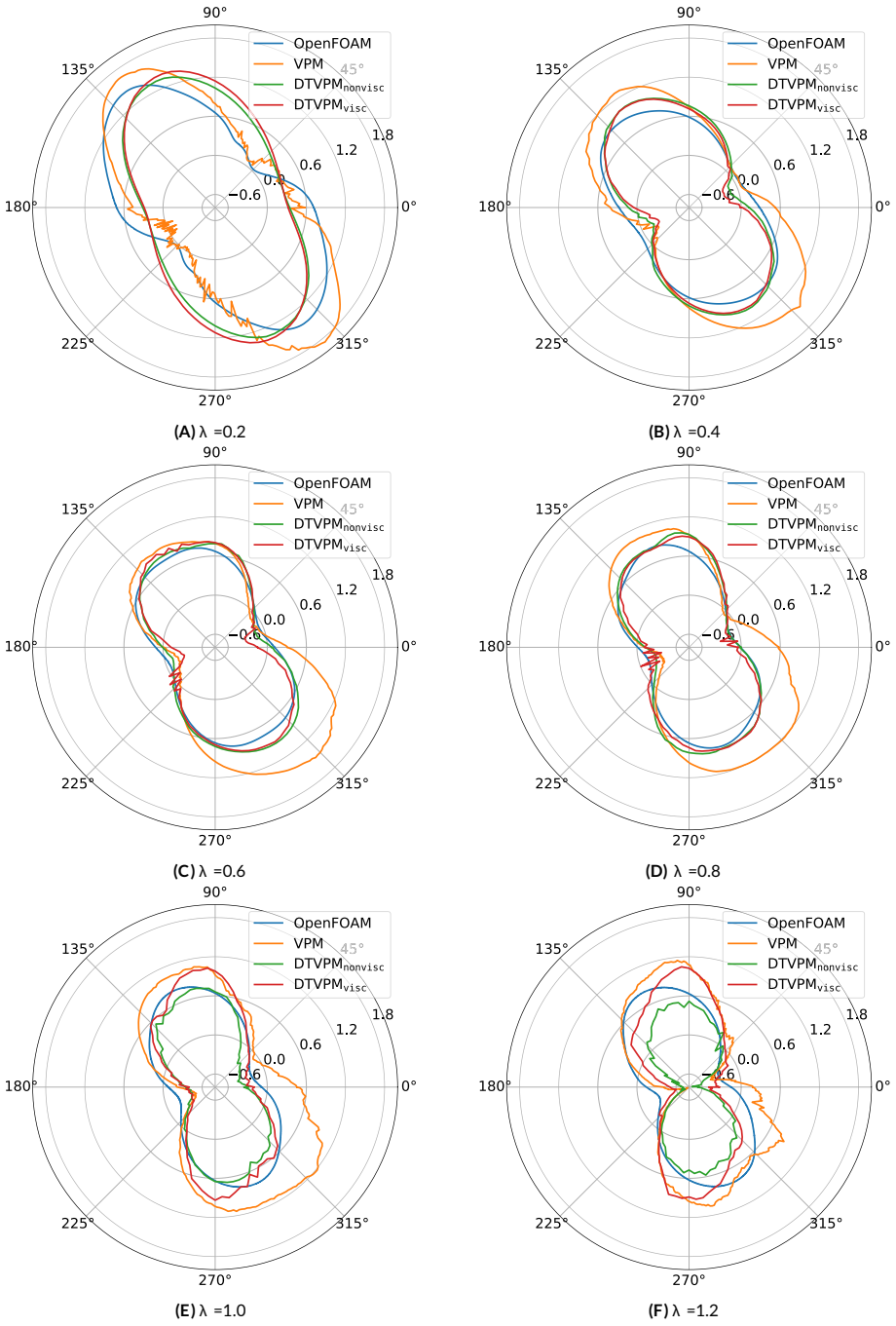

FIGURE 18 Torque coefficient over one revolution at different TSRs [Colour figure can be viewed at wileyonlinelibrary.com]

TABLE 3 Deviations of three implementations of VPM for torque coefficient over one revolution

Δc_q	Method	$\lambda = 0.2$	$\lambda = 0.4$	$\lambda = 0.6$	$\lambda = 0.8$	$\lambda = 1.0$	$\lambda = 1.2$	Average
Standard deviation σ	VPM	0.20	0.22	0.27	0.26	0.25	0.23	0.24
	DTVPM$_{nonvisc}$	0.32	0.14	0.09	0.10	0.10	0.21	0.16
	DTVPM$_{visc}$	0.37	0.17	0.14	0.11	0.17	0.24	0.20
Maximum	VPM	0.53	0.63	0.76	0.68	0.74	0.57	0.65
	DTVPM$_{nonvisc}$	0.47	0.28	0.20	0.26	0.33	0.83	0.39
	DTVPM$_{visc}$	0.57	0.38	0.31	0.25	0.34	0.44	0.38

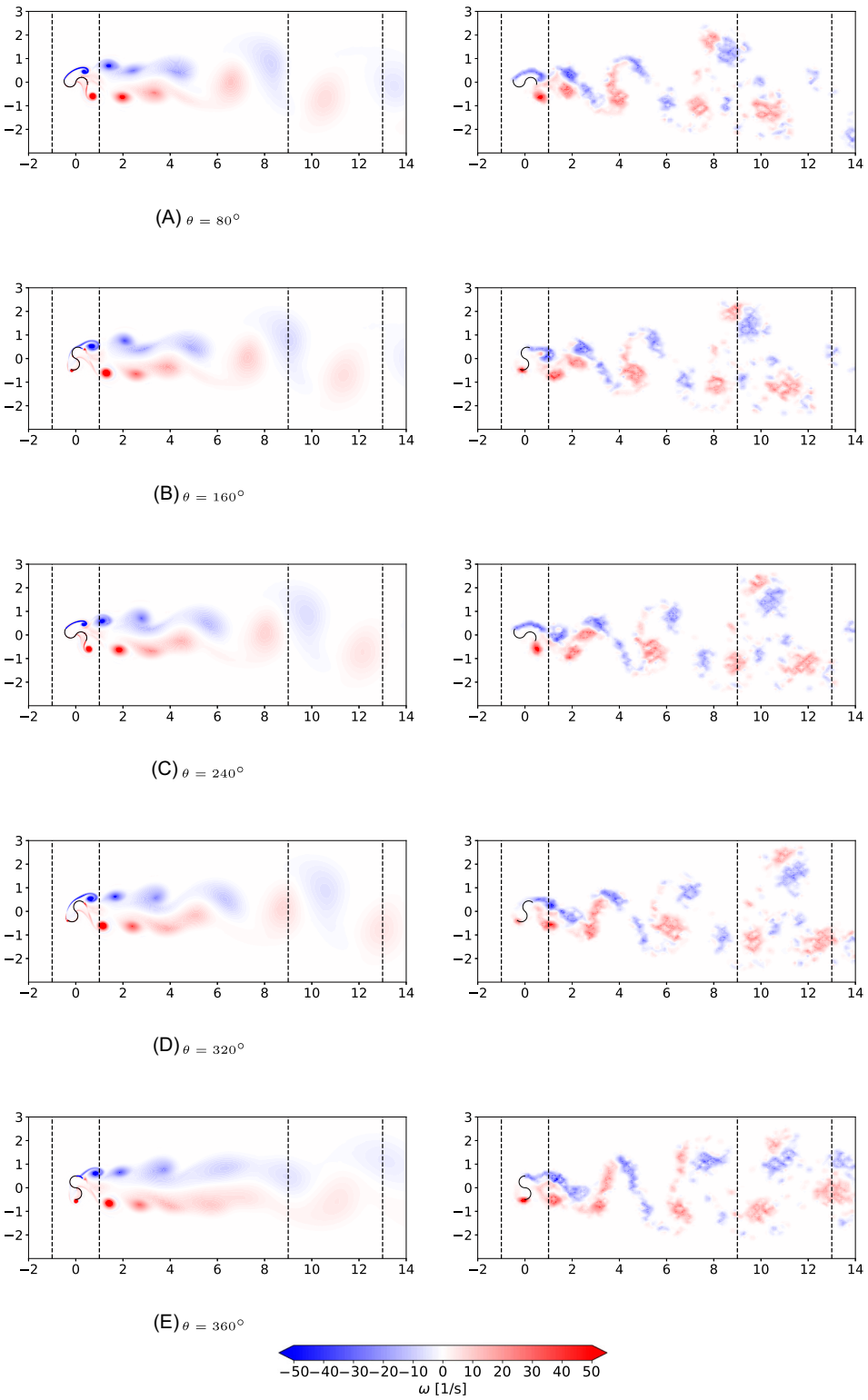

FIGURE 19 Comparison of flow features between OpenFOAM (left) and DTVPM with viscous correction (right) over one revolution, $\lambda = 0.8$, coordinate axis: x [m], y [m] [Colour figure can be viewed at wileyonlinelibrary.com]

from OpenFOAM, which corresponds to the vortex migration at x=9 m. Other quantifiable examples are U/U_∞ at x/R=26, θ=80° predicted by DTVPM being no more than 0.25 higher than that predicted by OpenFOAM, and U/U_∞ at x/R=26, θ=360° predicted by DTVPM being at most 0.52 higher than that predicted by OpenFOAM. Overall, discrepancies of the velocity magnitudes behind the rotor for OpenFOAM and DTVPM can be attributed to the limitations of DTVPM modeling in which the turbulence viscosity is absent.

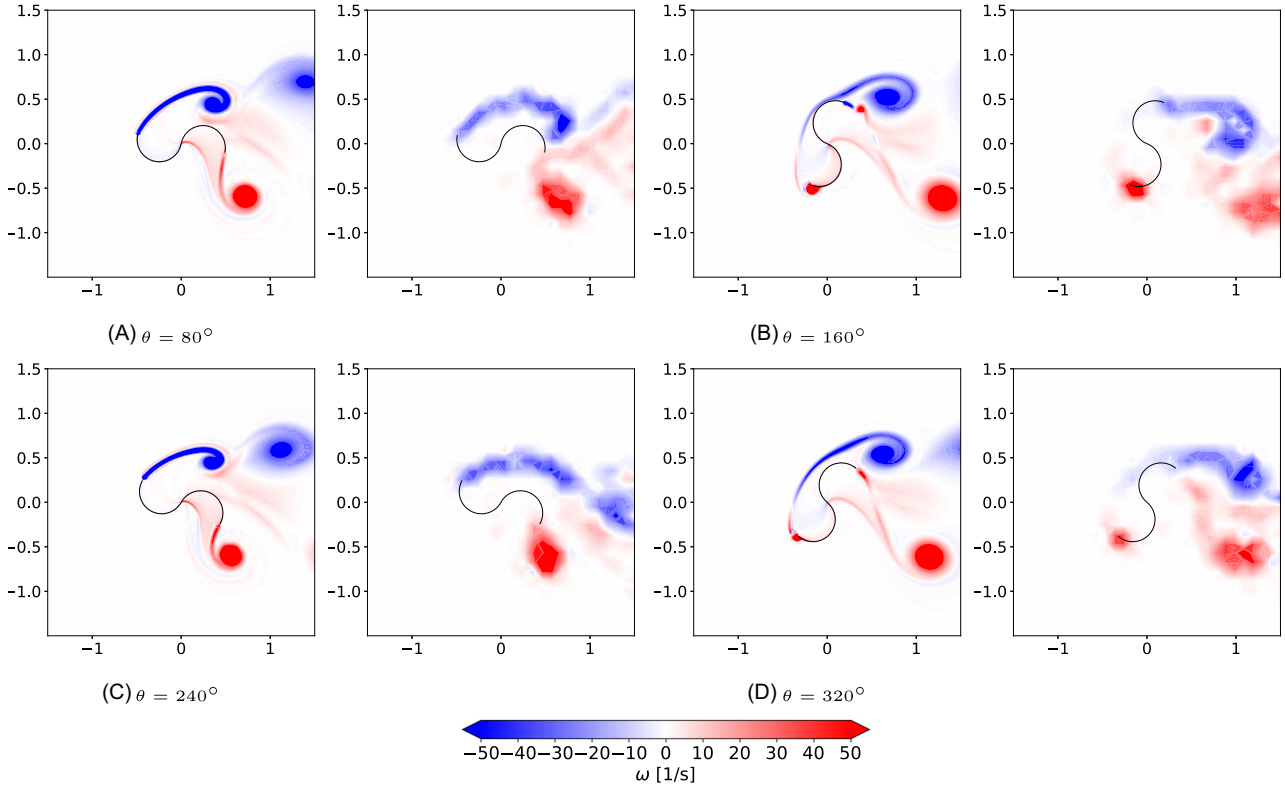

FIGURE 20 Vorticity fields at near-wake region from OpenFOAM (left) and DTVPM with viscous correction (right), $\lambda = 0.8$, coordinate axis: x [m], y [m] [Colour figure can be viewed at wileyonlinelibrary.com]

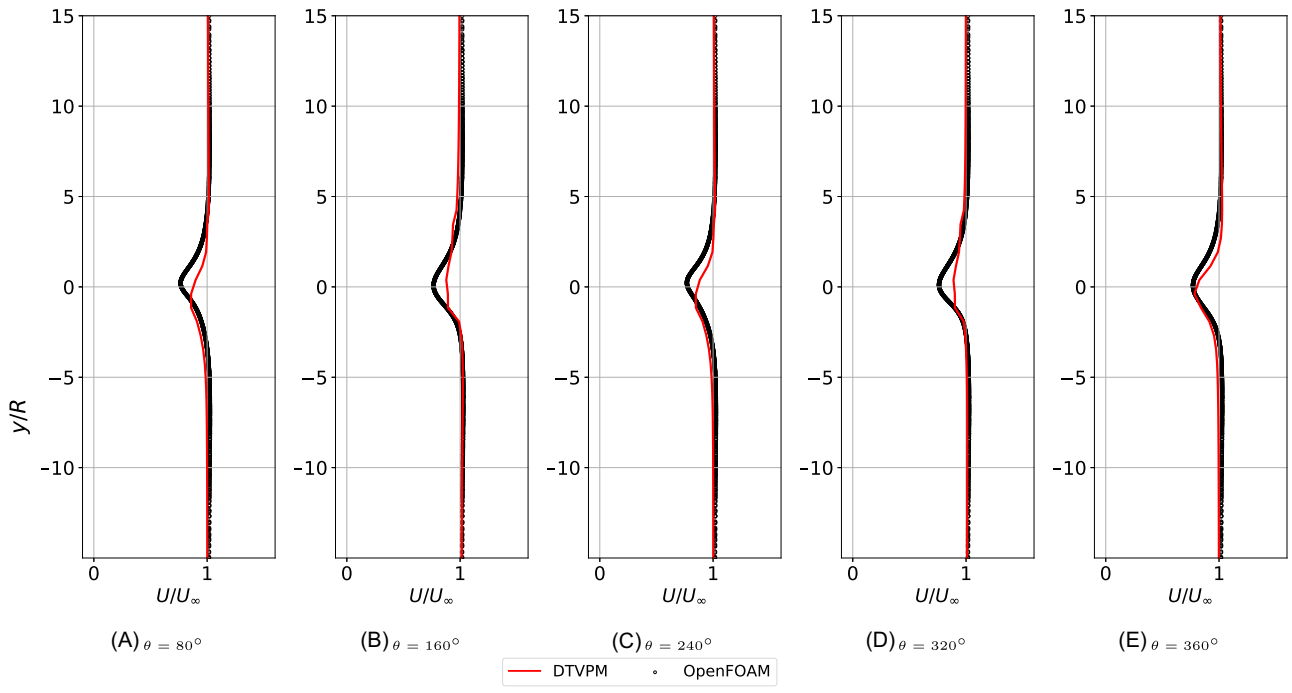

FIGURE 21 Velocity curve variations at x/R=-2 over one revolution, $\lambda = 0.8$ [Colour figure can be viewed at wileyonlinelibrary.com]

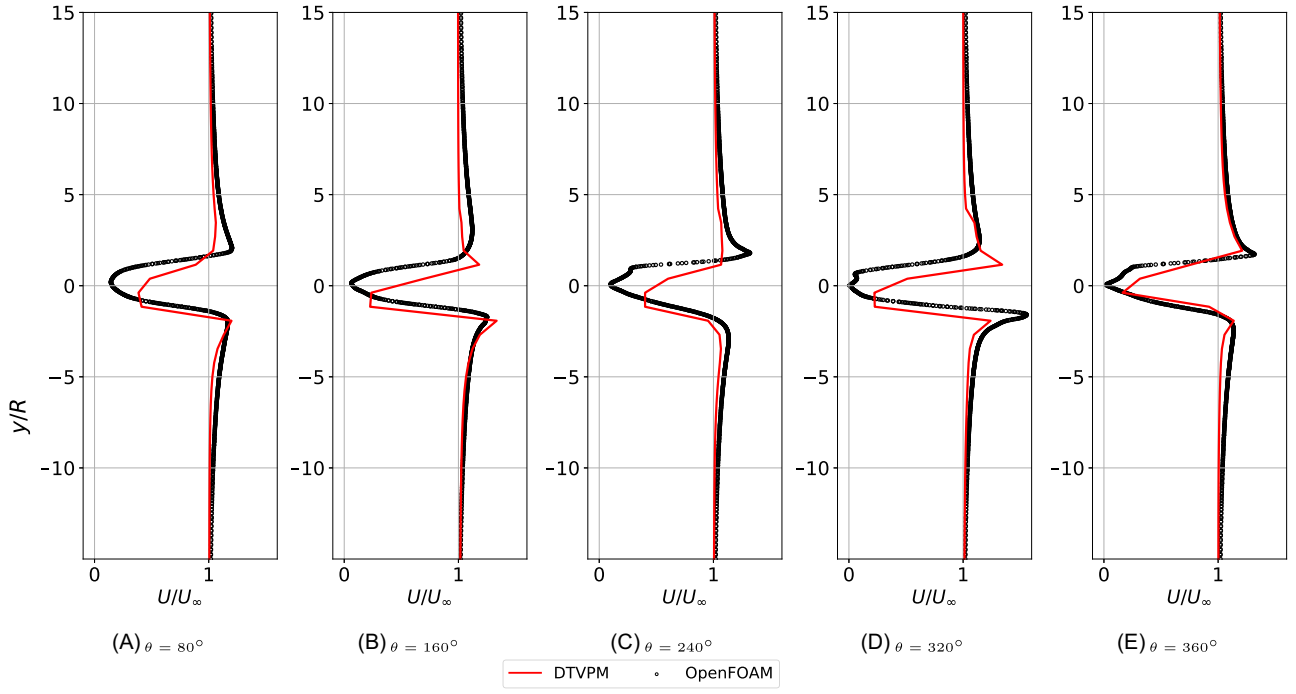

FIGURE 22 Velocity curve variations at x/R=2 over one revolution, $\lambda = 0.8$ [Colour figure can be viewed at wileyonlinelibrary.com]

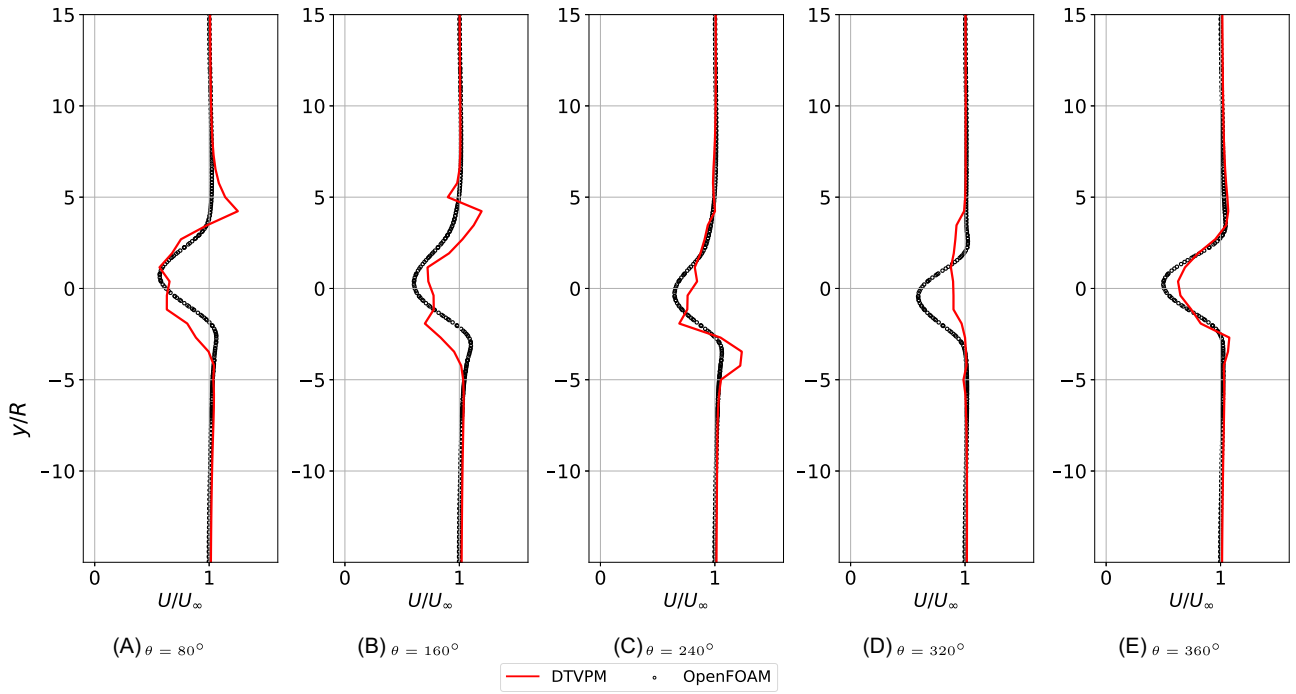

FIGURE 23 Velocity curve variations at x/R=18 over one revolution, $\lambda = 0.8$ [Colour figure can be viewed at wileyonlinelibrary.com]

3.6 | Computational efficiency

In this paper, one OpenFOAM simulation is executed on 20 cores per case. The computational domain size is 15 m × 25 m, discretized to 1.8e5 cells. The computer cluster operating system is Linux-based. The CPU processor used in this case is Intel(R) Xeon(R) E5-2640v4 with a frequency of 2.4 GHz. The DTVPM is computed as an order of $O(N_v^2)$ in serial processor, where N_v is the number of wake particles. Figure 25 compares

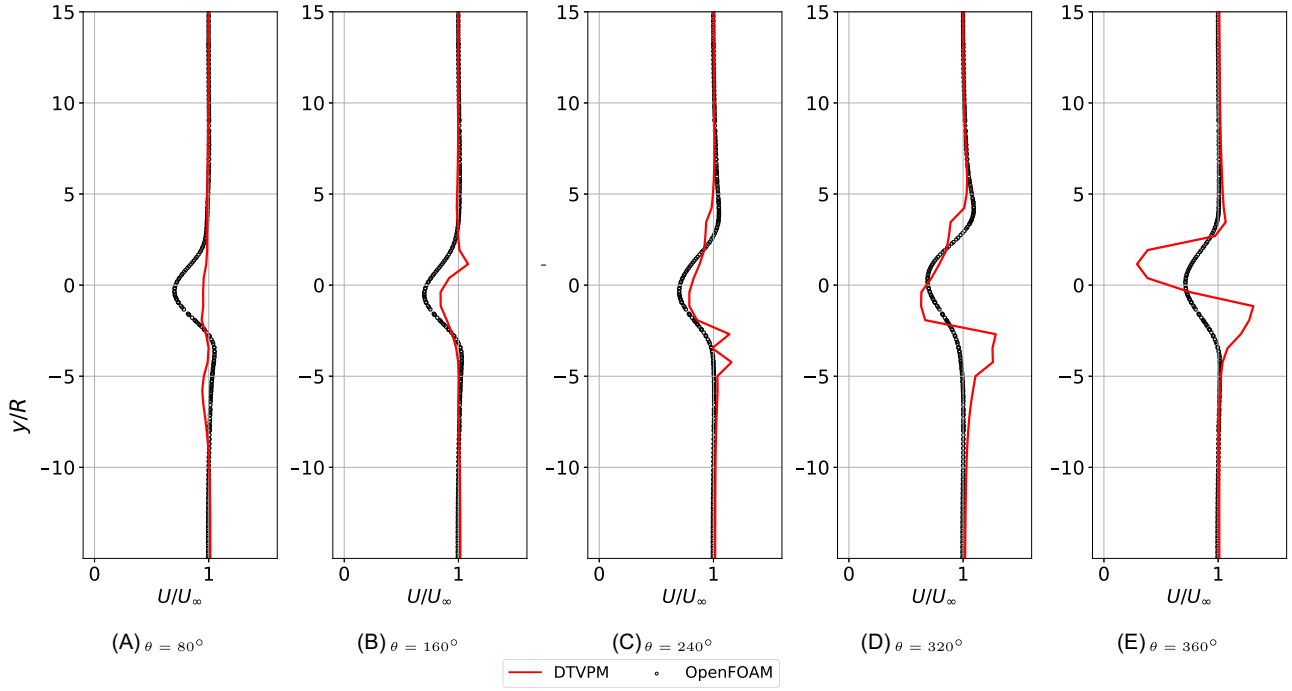

FIGURE 24 Velocity curve variations at x/R=26 over one revolution, $\lambda = 0.8$ [Colour figure can be viewed at wileyonlinelibrary.com]

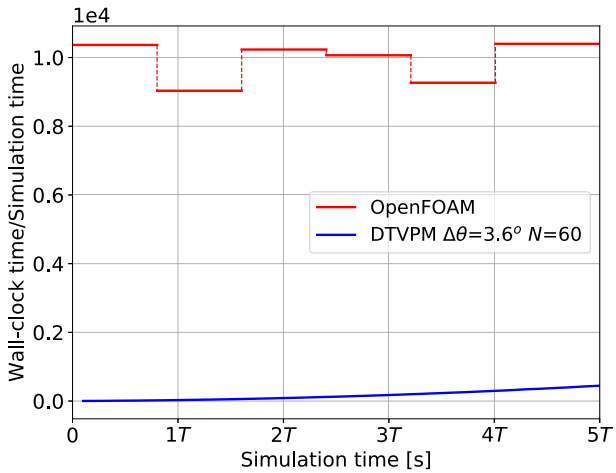

FIGURE 25 Computational efficiency of DTVPM and OpenFOAM [Colour figure can be viewed at wileyonlinelibrary.com]

DTVPM and OpenFOAM based on computational efficiency. The x axis represents simulation time for the first 5 revolutions. T is the rotation period of Savonius rotor. And y axis represents computational efficiency of numerical methods, which is characterized by the ratio of wall-clock time and simulation time. It is observed that the serial DTVPM simulation is about 1e4 times faster than the parallel OpenFOAM simulation. On the other hand, as indicated in Table 3, the maximum Δc_q predicted by DTVPM with viscous correction is 0.38 on average. Hence, under the premise of ensuring reasonable accuracy, DTVPM with viscous correction is a good alternative to study unsteady Savonius rotor.

4 | CONCLUSIONS

Vortex-based methods have been limited by small angle assumptions. To break the constraint, a VPM with double wake for a single-stage two-bladed semicircular Savonius rotor with no gap width is proposed at the beginning of the work. But it predicts asymmetrical forces on

the Savonius rotor. To avoid asymmetrical rotation, a double-trailing-edge-wake-modeling is applied to VPM, namely DTVPM. It is suitable for full period rotations, and independent from empirical parameters and post-corrected procedures. The location of trailing edge is illustrated to be essential to force calculation. DTVPM is effective to avoid asymmetrical force variations. Meanwhile, the computational accuracy is compared based on the selection of vortex core models. Results show that Vatistas and Lamb Oseen models predict a similar velocity distribution at $x/R = 2$. Vatistas model with $r_c = 0.012$ m has a maximum $\Delta(U/U_\infty)$ of 0.43 with a standard deviation of 0.08 at $x/R = 2$. In the far-wake region $x/R = 18$, Vatistas model with $r_c = 0.012$ m differs from OpenFOAM in a maximum $\Delta(U/U_\infty)$ of 0.12 with a standard deviation of 0.03. A remarkable finding is that the downstream velocity variation and power performance are dependent more on the choice of vortex core radius.

In general, the bound and latest wake vortex circulations are calculated at each time step. The wake vortex particles are convected with the local velocity. However, the assumption of inviscid flow cannot represent the practical local velocity. So, the viscous correction for tip vortices is implemented to simulate viscous effects near blade tips. And Δc_p is improved from -0.10 to 0.01 and from -0.27 to 0.01 at $\lambda = 1.0, 1.2$ after viscous correcting, respectively.

The proposed DTVPM with viscous correction is shown to be a cost-effective method by comparison with high-fidelity computational results for a number of Savonius motions. The serial DTVPM simulation with maximum Δc_q of 0.38 on average is around 1e4 times faster than the parallel OpenFOAM simulation. Power coefficient c_p of Savonius rotor is dependent on Reynolds number *Re*. The observed dependence can be attributed to the flow separation delay for high *Re* on the convex side of the rotor. Results of c_p from different methods show that OpenFOAM and DTVPM with viscous correction predict more stable results for varied tip speed ratio with standard deviation of 0.02. Through observations of flow characteristics for different phase angles at $\lambda = 0.8$, DTVPM is able to capture flow structures at $0 \le x/R \le 2$ but predicts a larger deflection of vortex position in y direction at $x/R \ge 2$. It can be improved by considering viscous effects at downstream.

ACKNOWLEDGEMENT

Jingna Pan gratefully acknowledges financial support from China Scholarship Council.

PEER REVIEW

The peer review history for this article is available at https://publons.com/publon/10.1002/we.2788.

ORCID

Jingna Pan https://orcid.org/0000-0001-5727-7105

REFERENCES

1. Blackwell B. Wind Tunnel Performance Data for Two- and Three-Bucket savonius turbine, SAND76-0131; 1977.
2. Saha UK, Thotla S, Maity D. Optimum design configuration of Savonius rotor through wind tunnel experiments. *J Wind Eng Ind Aerodyn*. 2008;96(8-9):1359-1375.
3. Jaohindy P, Ennamiri H, Garde F, Bastide A. Numerical investigation of airflow through a Savonius rotor. *Wind Energy*. 2014;17:853-868.
4. Aliferis AD, Jessen MS, Bracchi T, Hearst RJ. Performance and wake of a Savonius vertical-axis wind turbine under different incoming conditions. *Wind Energy*. 2019;22:1260-1273.
5. Kamoji M, Kedare SB, Prabhu S. Experimental investigations on single stage modified Savonius rotor. *Appl Energy*. 2009;86(7):1064-1073.
6. Kamoji M, Kedare SB, Prabhu S. Performance tests on helical Savonius rotors. *Renew Energy*. 2009;34(3):521-529.
7. Montelpare S, D'Alessandro V, Zoppi A, Ricci R. Experimental study on a modified Savonius wind rotor for street lighting systems: Analysis of external appendages and elements. *Energy*. 2018;144:146-158.
8. Tahani M, Rabbani A, Kasaeian A, Mehrpooya M, Mirhosseini M. Design and numerical investigation of Savonius wind turbine with discharge flow directing capability. *Energy*. 2017;130:327-338.
9. Sarma J, Jain S, Mukherjee P, Saha UK. Hybrid/Combined Darrieus-Savonius Wind Turbines: Erstwhile Development and Future Prognosis. *J Sol Energy Eng*. 2021;143(5):50801.
10. Liang X, Fu S, Ou B, Wu C, Chao CYH, Pi K. A computational study of the effects of the radius ratio and attachment angle on the performance of a Darrieus-Savonius combined wind turbine. *Renew Energy*. 2017;113:329-334.
11. Peters DA. Two-dimensional incompressible unsteady airfoil theory–An overview. *J Fluids Struct*. 2008;24(3):295-312.
12. Lighthill M. A New Approach to Thin Aerofoil Theory. *Aeronaut Q*. 1951;3(3):193-210.
13. Theodorsen T. General theory of aerodynamic instability and the mechanism of flutter. *NACA Rep*. 1935:496.
14. Wagner H. Über die Entstehung des dynamischen Auftriebes von Tragflügeln. *Z Angew Math Mech*. 1925;5(1):17-35.
15. Tollmien W, Schlichting H, Görtler H, Riegels FW. Tragflügeltheorie, Ludwig Prandtl Gesammelte Abhandlungen. 322–345; 1918.
16. Lanchester FW. *Aerodynamics, constituting the first volume of a complete work on aerial flight*, A. Constable & Co., Ltd; 1907.
17. Korprasertsak N, Leephakpreeda T. Analysis and optimal design of wind boosters for Vertical Axis Wind Turbines at low wind speed. *J Wind Eng Ind Aerodyn*. 2016;159:9-18.
18. Kacprzak K, Liskiewicz G, Sobczak K. Numerical investigation of conventional and modified Savonius wind turbines. *Renew Energy*. 2013;60:578-585.
19. Shigetomi A, Murai Y, Tasaka Y, Takeda Y. Interactive flow field around two Savonius turbines. *Renew Energy*. 2011;36:536-545.
20. Gao J, Liu H, Lee J, Zheng Y, Guala M, Shen L. Large-eddy simulation and Co-Design strategy for a drag-type vertical axis hydrokinetic turbine in open channel flows. *Renew Energy*. 2022;181:1305-1316.

21. Lee J, Musa M, Feist C, Gao J, Shen L, Guala M. Wake Characteristics and Power Performance of a Drag-Driven in-Bank Vertical Axis Hydrokinetic Turbine. *Energies*. 2019;12(19):3611.
22. Dobrev I, Massouh F. CFD and PIV investigation of unsteady flow through Savonius wind turbine. *Energy Procedia*. 2011;6:711-720.
23. Han Y, Ding G, He Y, Wu J, Le J. Assessment of the IDDES method acting as wall-modeled LES in the simulation of spatially developing supersonic flat plate boundary layers. *Eng Appl Comput Fluid Mech*. 2018;12(1):89-103.
24. Elkhoury M, Kiwata T, Nagao K, Kono T, ElHajj F. Wind tunnel experiments and Delayed Detached Eddy Simulation of a three-bladed micro vertical axis wind turbine. *Renew Energy*. 2018;129:63-74.
25. Antar E, Elkhoury M. Parametric sizing optimization process of a casing for a Savonius Vertical Axis Wind Turbine. *Renew Energy*. 2019;136:127-138.
26. Ramesh K, Gopalarathnam A, Granlund K, Ol MV, Edwards JR. Discrete-vortex method with novel shedding criterion for unsteady airfoil flows with intermittent leading-edge vortex shedding. *J Fluid Mech*. 2014;751:500-538.
27. Wang C, Eldredge JD. Low-order phenomenological modeling of leading-edge vortex formation. *Theor Comput Fluid Dyn*. 2013;27:577-598.
28. Hemati MS, Eldredge JD, Speyer JL. Improving vortex models via optimal control theory. In: 51st AIAA Aerosp. Sci. Meet. Incl. New Horizons Forum Aerosp. Expo; 2014.
29. Ogawa T. Theoretical study on the flow about savonius rotor. *J Fluid Eng*. 1984;106(1):85-91.
30. Li Y, Çalışal SM. A discrete vortex method for simulating a stand-alone tidal current turbine: modeling and validation. *J Offshore Mech Arct Eng*. 2010;132(3):31102.
31. Li Y, Çalışal SM. Numerical analysis of the characteristics of vertical axis tidal current turbines. *Renew Energy*. 2010;35:435-442.
32. Sale D, Aliseda A, Li Y. Simulation of hydrokinetic turbines in turbulent flow using Vortex Particle Methods. In: Proc. Mar. Energy Technol Symp.; 2014.
33. Hejlesen MM, Rasmussen JT, Larsenb A, Walther JH. On estimating the aerodynamic admittance of bridge sections by a mesh-free vortex method. *J Wind Eng Ind Aerodyn*. 2015;146:117-127.
34. Chawdhury S, Morgenthal G. Flow reproduction using Vortex Particle Methods for simulating wake buffeting response of bluff structures. *J Wind Eng Ind Aerodyn*. 2016;151:122-136.
35. Jin G, Zou L, Jiang Y, Zong Z, Sun Z. A circle theorem technique to handle 2-D flows around arbitrary cylinders in discrete vortex method. *J Wind Eng Ind Aerodyn*. 2021;209:104496.
36. Katz J, Plotkin A. Low-speed aerodynamics; 2001.
37. Vatistas GH, Kozel V, Mih WC. A Simpler Model for Concentrated Vortices. *Exp Fluids*. 1991;11(1):73-76.
38. Abutunis AM, Menta VG. Comprehensive Parametric Study of Blockage Effect on the Performance of Horizontal Axis Hydrokinetic Turbines. *Energies*. 2022;15(7):2585.
39. Kinsey T, Dumas G. Impact of channel blockage on the performance of axial and cross-flow hydrokinetic turbines. *Renew Energy*. 2017;103:239-254.
40. Hald O, del Prete V. Convergence of Vortex Methods for Euler's Equations. *Math Comput*. 1978;32(143):791-809.
41. Kaufmann W. Uber die Ausbreitung kreiszlindrischer Wirbel in zahen Flussigkeiten. *Ing Arch*. 1962;31(1):1-9.
42. Lamb H. *Hydrodynamics*, 6th ed. Cambridge Univ. Press; 1932.
43. Oseen CW. Uber Wirbelbewegung in Einer Reibenden Flussigkeit. *Ark J Mat Astrom Fys*. 1912;7:14-21.
44. Bhagwat MJ, Leishman JG. Generalized viscous vortex model for application to free-vortex wake and aeroacoustic calculations. In: 58th *Annu Forum Proceedings-American Helicopter Soc*; 2002.

How to cite this article: Pan J, Ferreira C, A van Zuijlen. Estimation of power performances and flow characteristics for a Savonius rotor by vortex particle method. *Wind Energy*. 2022;1-22. doi:10.1002/we.2788